Research Square

Preprints are preliminary reports that have not undergone peer review.
They should not be considered conclusive, used to inform clinical practice,
or referenced by the media as validated information.

# UAV-Based Thermal Remote Sensing in Desert Environments: Methodological Framework and Experimental Analysis of the Casma Valley Geoglyphs, Peru

**Gabriele Ciccone**
National Research Council
**Nicodemo Abate**
National Research Council
**Angel Sanchez Borjas**
Pontificia Universidad Católica del Perú
**Jeff Contreras**
Apu Space
**Ivan Ghezzi**
Ministry of Culture
**Rosa Lasaponara**
National Research Council
**Nicola Masini**
nicola.masini@cnr.it
National Research Council

**Research Article**

**Keywords:** Archaeological remote sensing, geoglyphs, Drone thermal imaging, Diurnal thermal cycle, Local Indicators of Spatial Association

**Posted Date:** August 19th, 2026

**DOI:** https://doi.org/10.21203/rs.3.rs-10479848/v1

**License:** This work is licensed under a Creative Commons Attribution 4.0 International License.
Read Full License

**Additional Declarations:** No competing interests reported.

# UAV-Based Thermal Remote Sensing in Desert Environments: Methodological Framework and Experimental Analysis of the Casma Valley Geoglyphs, Peru

**Gabriele Ciccone[1], Nicodemo Abate[1], Angel Sanchez Borjas[2], Jeff Contreras[3], Ivan Ghezzi [4], Rosa Lasaponara[5], Nicola Masini[1*]**

1 CNR-ISPC (Istituto di Scienze del Patrimonio Culturale), C. da S. Loya, Tito Scalo (PZ), Italy. https://orcid.org/0000-0002-8804-5718
2 Programa de Estudios Andinos, Escuela de Posgrado, Pontificia Universidad Católica del Perú, Lima, Perú.
3 Apu Space, Amazonas, Peru, https://orcid.org/0000-0002-9258-9638
4 Unidad Ejecutora Chankillo, Ministerio de Cultura del Peru, Peru.
5 CNR-IMIOT (Istituto di Metodologie di Analisi Ambientale), C. da S. Loya, Tito Scalo (PZ), https://orcid.org/0000-0002-1287-646X

(*) Corresponding author: nicola.masini@cnr.it

**Abstract** Thermal infrared remote sensing has become an increasingly important tool for archaeological prospection because it enables the detection of subtle thermal anomalies associated with buried and surface archaeological features. Previous studies have generally concluded that thermal surveys conducted during nighttime provide the most favourable conditions for archaeological detection, whereas daytime acquisitions are considered less effective due to the masking influence of solar heating. However, these conclusions were largely established using earlier generations of thermal sensors characterized by limited spatial and radiometric resolutions. The advent of UAV-borne thermal sensors offers new opportunities to re-evaluate the temporal dynamics of archaeological thermal signatures and to investigate whether favourable detection conditions may also occur during daytime periods. In this study, we systematically investigate the complete diurnal evolution of thermal signatures associated with the desert geoglyphs in Casma Valley, northern Peru, using ultra-high-resolution UAV-based thermal imagery. Desert geoglyphs provide an exceptional natural laboratory because their thermal response is controlled primarily by intrinsic material properties rather than by vegetation stress or soil moisture anomalies that often complicate the interpretation of buried archaeological features. Repeated thermal acquisitions were performed at three representative periods of the entire diurnal cycle, enabling the characterization of the temporal behaviour of both positive and negative geoglyphs and the assessment of the physical mechanisms governing their thermal responses. The results reveal pronounced temporal variability in archaeological thermal contrasts and demonstrate that the detectability of geoglyphs is strongly dependent on the time of acquisition. Contrary to the traditional assumption that nocturnal conditions are invariably optimal, significant thermal contrasts are also observed during specific daytime periods, indicating that archaeological detectability is controlled by the interplay between material thermal properties and environmental forcing rather than by illumination conditions alone. Moreover, positive and negative geoglyphs exhibit distinct and predictable thermal trajectories, reflecting differences in their construction techniques and material composition. These findings provide new insights into the physical processes governing archaeological thermal signatures and challenge long-standing paradigms regarding optimal acquisition times for thermal archaeological prospection. Beyond the specific case of Peruvian geoglyphs, this work establishes a process-based framework for the interpretation of archaeological thermal anomalies and contributes to the development of more effective and transferable UAV thermal remote-sensing methodologies for the detection and monitoring of cultural heritage in arid and semi-arid environments.

**Keywords: Archaeological remote sensing; geoglyphs; Drone thermal imaging; Diurnal thermal cycle; Local Indicators of Spatial Association**

## 1. Introduction

Over the past decade, Unmanned Aerial Vehicles (UAVs), commonly referred to as drones, have profoundly transformed remote sensing by enabling the acquisition of ultra-high-resolution imagery with unprecedented temporal flexibility. By operating at low altitudes and providing centimetre-scale spatial resolution, UAV platforms effectively bridge the observational gap between satellite and conventional airborne remote sensing and direct field investigations. This capability is particularly relevant for archaeological prospection, where the detection of subtle manifestations of buried or partially exposed archaeological remains often requires observations at spatial scales beyond the capabilities of traditional Earth-observation systems.

The increasing availability of lightweight sensors has fostered the development of multi-sensor UAV-based approaches that integrate complementary spectral domains for archaeological investigations. Beyond conventional RGB imaging, multispectral sensors operating in the visible and near-infrared (VNIR) regions of the electromagnetic spectrum can reveal variations in vegetation vigour, soil composition, moisture conditions, and surface roughness induced by subsurface archaeological features. Since the early 2000s, multispectral satellite imagery, frequently combined with virtual globes such as Google Earth, has been successfully employed to identify previously unknown archaeological sites and reconstruct ancient landscapes (Lasaponara and Masini, 2007; Klokočník et al., 2011; Agapiou et al., 2016; Tapete and Cigna, 2019).

Among the various sensing technologies available for archaeological prospection, thermal infrared (TIR) remote sensing occupies a unique position because it directly measures the emitted radiance of the Earth's surface and therefore provides information on the thermodynamic state of near-surface materials. Archaeological features such as walls, foundations, roads, ditches, cavities, and anthropogenic deposits often possess physical properties—including thermal conductivity, density, porosity, heat capacity, and moisture retention characteristics—that differ significantly from those of the surrounding sediments. These differences alter the local surface energy balance and generate measurable thermal anomalies that may be exploited for archaeological detection (Casana et al., 2017; Agudo et al., 2018; Hill et al., 2020; Hollesen et al., 2023; Ciccone, 2024).

The formation and evolution of archaeological thermal anomalies are governed by the interaction of radiative forcing, conductive heat transfer, atmospheric exchanges, and soil moisture dynamics. Consequently, surface temperatures are influenced by environmental factors such as vegetation cover, soil composition, moisture content, topography, and local climate (Agudo et al., 2018; James et al., 2020; Ciccone, 2024).

A key parameter governing these processes is thermal inertia, which describes a material's ability to absorb, store, and release heat. Materials with high thermal inertia warm and cool more slowly than those with low thermal inertia, generating distinct diurnal thermal trajectories. Differences in thermal inertia between archaeological materials and surrounding sediments therefore produce measurable thermal contrasts that can be exploited for archaeological detection (Cracknell and Kappelmeyer, 1992; Parcak, 2009; Casana et al., 2017).

Previous studies have generally concluded that thermal surveys conducted shortly after sunset or before sunrise provide the most favourable conditions for archaeological detection in bare-soil environments because differential cooling maximizes thermal contrast between archaeological materials and surrounding sediments (Scollar et al., 1990; Casana et al., 2014, 2017; Hill et al., 2020). Consequently, daytime acquisitions have traditionally been regarded as less effective because strong solar heating increases surface thermal heterogeneity and may mask subtle archaeological anomalies.

However, this widely accepted paradigm may partly reflect the technological limitations of earlier thermal imaging systems. Previous generations of sensors were characterized by relatively coarse spatial resolution, lower radiometric sensitivity, and reduced thermal stability, which constrained their ability to detect fine-scale thermal gradients under dynamically changing daytime conditions. Recent advances in uncooled microbolometer technology, characterized by sub-decikelvin thermal sensitivity, improved radiometric accuracy, and centimetre-scale spatial resolution when deployed on UAV platforms, have significantly enhanced the capability to resolve subtle thermal anomalies (Aubrecht et al., 2016; Pande-Chhetri et al., 2017; Peppa et al., 2021).

Despite these technological advances, the temporal evolution of archaeological thermal signatures over an entire diurnal cycle remains poorly understood. Most previous investigations have relied on a limited number of acquisition times and have largely focused on nocturnal conditions. Consequently, there is still no comprehensive process-based framework explaining how the detectability of archaeological features varies as a function of

environmental forcing, material properties, and time of acquisition. The assumption that nighttime observations invariably provide the optimal conditions for archaeological detection therefore warrants critical re-evaluation.

To address these knowledge gaps, the present study investigates the complete diurnal evolution of thermal signatures associated with desert geoglyphs in northern Peru using ultra-high-resolution UAV thermal imagery. Desert geoglyphs provide an exceptional natural laboratory because their thermal response is governed primarily by intrinsic material properties rather than by vegetation stress or soil moisture anomalies that commonly complicate the interpretation of buried archaeological remains.

Unlike subsurface remains, geoglyphs are surface or near-surface constructions whose visibility depends largely on differences in thermal inertia, emissivity, heat capacity, and thermal conductivity between construction materials and surrounding sediments. Consequently, they provide a direct means of investigating the fundamental physical mechanisms governing archaeological thermal signatures.

Arid environments further enhance the suitability of this experimental setting. Sparse or absent vegetation minimizes masking effects and allows the thermal response of archaeological materials to be observed directly. Moreover, deserts experience some of the largest diurnal temperature amplitudes on Earth, frequently exceeding 30–40 °C within a single day. Such pronounced heating and cooling cycles amplify differences in the thermal behaviour of materials and provide ideal conditions for investigating the temporal dynamics of archaeological thermal anomalies.

Desert geoglyphs are also representative of a broad class of archaeological features distributed across drylands worldwide, including the Atacama Desert, the Peruvian coastal deserts, the Arabian Peninsula, the Sahara, Central Asia, and the deserts of the southwestern United States (Briones 2006; Lambers 2006; Masini et al. 2016; Sakai et al. 2024).

Although these sites differ culturally and chronologically, they share comparable environmental conditions and construction principles, making them an excellent benchmark for developing transferable thermal remote-sensing methodologies.

A particularly rigorous validation framework is provided by the coexistence of positive and negative geoglyphs. Because these two classes are produced through opposite construction processes—material accumulation versus material removal—they are expected to exhibit distinct thermal behaviours and contrasting diurnal trajectories. Demonstrating that thermal infrared data can reliably discriminate between them throughout the diurnal cycle would provide strong evidence that the proposed methodology is sensitive to archaeological morphology, material composition, and construction techniques rather than merely detecting generic surface temperature anomalies.

This study addresses two fundamental questions: (i) how archaeological thermal signatures evolve throughout the diurnal temperature cycle and when they reach maximum detectability; and (ii) whether different classes of geoglyphs exhibit distinct thermal responses as a consequence of their contrasting construction techniques and thermophysical properties.

Accordingly, we test four hypotheses: (i) archaeological thermal contrast does not consistently peak during nocturnal periods; (ii) the timing and magnitude of thermal anomalies are governed primarily by differences in thermophysical properties between geoglyphs and the surrounding sediments; (iii) positive and negative geoglyphs exhibit distinct and predictable diurnal thermal trajectories; and (iv) modern UAV thermal sensors can detect significant archaeological anomalies during specific daytime periods as effectively as during traditional nocturnal observation windows.

By characterizing the complete diurnal thermal cycle of desert geoglyphs, this study provides a process-based framework for optimizing UAV thermal surveys and improving the interpretation of archaeological thermal anomalies in arid and semi-arid environments.

## 2 Materials and Methods

### 2.1 Study area

The Casma Valley, located on Peru's north-central coast in the department of Ancash, represents one of the most arid regions of the South American continent. Bounded by the Pacific Ocean to the west and the foothills of the Andes to the east, the valley forms part of the extensive coastal desert belt stretching from southern Ecuador to northern Chile. Annual rainfall rarely exceeds 20 mm, and most of the valley's water derives from seasonal runoff and meltwater originating in the Cordillera Negra. This hydrological dependence creates a sharp contrast between the barren pampas and the narrow, fertile alluvial plain nourished by the Casma river.

Climatically, the region is influenced by the cold Humboldt Current, which promotes atmospheric stability and frequent coastal fogs (garúa) while suppressing convective rainfall. Average temperatures remain mild throughout the year (18–24 °C), yet the lack of precipitation and high evaporation rates produce hyper-arid soil conditions. Vegetation outside irrigated zones is extremely sparse, consisting mainly of xerophytic shrubs and ephemeral grasses. Periodic El Niño events occasionally disrupt this equilibrium, causing floods and sediment deposition that have repeatedly reshaped the lower valley. Such a setting, characterized by intense daytime insolation and rapid nocturnal cooling, provides an ideal environment for thermal contrast observations.

This was precisely the context selected for our experimental test campaign, aimed at evaluating the use of drone-mounted thermal sensors for detecting temperature variations that may enhance the identification and distinction of geoglyphs of different types.

Archaeologically, the Casma and Sechín valleys have long been recognized as key centers for the study of Peru's pre-Hispanic coastal civilizations (Burger 1992; Pozorki & Pozorski, 2011; Tello 1956; Wilson, 1995). Numerous monumental sites, including Chankillo, Sechín Alto, Cerro Sechín, Las Aldas, and El Purgatorio, underscore the region's cultural significance.

The specific area chosen for this research lies on the broad alluvial plain of the Huaraspampa ravine, which begins at the southern end of the gorge formed by the Colorado and Mirador hills (Fig. 1). The zone is well known for its geoglyphs, architectural remains, and traces of pre-Hispanic roadways, distributed around a long, yellowish hill emerging in the center of the plain—an evident landmark during the pre-Hispanic period (Pineda Quevedo, 2020; Sanchez & Ghezzi, 2025).




**Fig. 1** Study area and location of the investigated geoglyphs in the Huaraspampa Plain, Casma Valley, Peru

## 2.2. Methods and Experimental design

This study investigates two complementary objectives: (i) characterizing the evolution of archaeological thermal signatures throughout the diurnal temperature cycle and identifying the periods of maximum detectability; and (ii) determining whether different classes of geoglyphs exhibit distinct thermal responses as a consequence of their contrasting construction techniques and thermophysical properties.

The first objective stems from the recognition that the detectability of archaeological features in thermal imagery is highly dependent on the timing of data acquisition. Surface temperature patterns are governed by the interaction of multiple environmental factors, including soil composition, moisture content, local microclimate, altitude, latitude, vegetation cover, and proximity to coastal or wetland environments. Together, these factors control both the amplitude and phase of the diurnal temperature cycle, thereby influencing the magnitude and timing of archaeological thermal contrasts (Agudo et al., 2018; James et al., 2020; Ciccone, 2024).

The second objective examines the hypothesis that differences in geoglyph construction result in distinct thermophysical properties and, consequently, contrasting thermal responses. Geoglyphs can be broadly classified into two principal categories:

- Positive geoglyphs, created by the accumulation of material, such as stones, gravel, or earth, to form raised patterns or structures.
- Negative geoglyphs, produced by removing the upper soil layer to expose a lighter-colored subsurface, thereby creating visual contrast. In many cases, the excavated material is deposited along the margins of the figure, forming low embankments that further enhance visibility (Masini et al., 2016a).

These contrasting construction techniques are expected to produce different thermal behaviours. Stone accumulations generally possess greater thermal mass and thermal inertia than the surrounding sediments, allowing them to absorb and release heat at different rates. Conversely, the exposed substrate within negative geoglyphs may differ from the surrounding terrain in terms of thermal conductivity, heat capacity, emissivity, grain size, and moisture retention characteristics. As a result, positive and negative geoglyphs are expected to exhibit distinct heating and cooling trajectories throughout the diurnal cycle, generating characteristic thermal signatures that may facilitate their discrimination and interpretation.

In accordance with the objectives of the investigation, this study adopts a multi-temporal approach aimed at determining whether different classes of geoglyphs exhibit distinct optimal observation periods and whether significant archaeological thermal contrasts can also be observed during daytime conditions.

Because positive and negative geoglyphs possess different thermophysical properties, each class may reach maximum thermal contrast with the surrounding terrain at different times of the day. Consequently, identifying a single optimal acquisition window a priori may lead to an incomplete characterization of archaeological thermal behaviour.

To investigate the diurnal evolution of geoglyph thermal signatures, a multi-sensor UAV campaign was conducted in the Casma Valley, Peru. The survey employed a mid-size multirotor platform (DJI Matrice 350 RTK) capable of carrying multiple imaging payloads.

Two sensors were deployed in separate missions:

1. DJI Zenmuse H20T equipped with: (i) TIR camera, an uncooled VOx microbolometer operating in the 7.5–13.5 μm spectral range, with a spatial resolution of 640 × 512 pixels and a frame rate of 30 Hz, (ii) RGB camera with an image resolution of 4000 × 3000 pixels for the production of high-resolution orthophotography.
2. Multispectral camera: Sentera AGX710 acquiring five spectral bands: Blue (446 nm), Green (548 nm), Red (650 nm), Red Edge (720 nm), and Near Infrared (840 nm).

RGB and multispectral acquisitions were performed around local solar noon under stable illumination conditions. Thermal missions were conducted at three representative periods of the diurnal cycle:

- Pre-dawn (~05:30): following prolonged nocturnal cooling;
- Midday (~12:00): during maximum incoming solar radiation;
- Post-sunset (~19:00): during the initial surface cooling phase.

The rationale for this acquisition strategy is based on the expectation that geoglyph materials and surrounding sediments possess different thermal inertias and therefore exhibit different heating and cooling rates. During the pre-dawn period, materials with greater thermal inertia are expected to retain residual heat and appear as relatively warmer anomalies. Conversely, during the post-sunset period, differential cooling rates may generate reversed thermal contrasts. Midday acquisitions were included to investigate whether thermal sensors are capable of resolving archaeological thermal anomalies even under conditions of strong solar forcing.

### 2.3 Data acquisition and processing

Thermal missions were flown at an altitude of 75 m above ground level, corresponding to a ground sampling distance of approximately 7.3 cm pixel$^{-1}$. Full radiometric information was recorded for each image. Concurrently, an on-site meteorological station continuously measured air temperature, relative humidity, and wind speed, enabling the direct assessment of the relationship between environmental conditions and surface thermal behaviour.

Each flight generated more than one thousand overlapping images. Thermal, RGB, and multispectral datasets were processed through photogrammetric workflows using Agisoft Metashape Professional (v.2.2.2) and WebODM (v.2.9.2). Both software packages were employed to generate georeferenced orthomosaics and to evaluate the robustness and reproducibility of the thermal reconstruction workflow.

The photogrammetric processing included image alignment, camera optimization, dense point-cloud generation, and orthomosaic production. The principal processing parameters adopted in both software environments are summarized in Table 1.

Both software packages were used to generate georeferenced thermal orthomosaics for each time slot.

| | Agisoft Metashape 2.2.2. | WebODM 2.9.2 |
|---|---|---|
| Alignment images parameters | Accuracy: High<br>Generic preselection: Yes<br>Reference preselection: Source<br>Key point limit: 40,000<br>Key point limit per Mpx : 1,000<br>Tie point limit: 10,000<br>Exclude stationary tie points: Yes<br>Guided image matching: No<br>Adaptive camera model fitting: No | Feature-quality: ultra<br>Feature-type: hahog<br>Force-gps: true<br>Matcher-type: bruteforce<br>Matcher-neighbors: false Merge: all |
| 3D model reconstruction parameters | Depth maps<br>Quality: High<br>Filtering mode: Mild<br>Max neighbors: 16<br><br>Reconstruction parameters<br>Surface type: Arbitrary<br>Source data: Depth maps<br>Interpolation: Enabled<br>Strict volumetric masks: No | Mesh-octree-depth: 11<br>Mesh-size: 200000<br>PC-quality: ultra<br>Sfm-algorithm: planar |
| Orthomosaic reconstruction parameter | Blending mode: Mosaic<br>Surface: Model<br>Enable hole filling: Yes<br>Enable ghosting filter: No | Dem-resolution: 2.0 Dsm: true Dtm: true<br>Orthophoto-resolution: 0.5 |

**Tab. 1** Photogrammetric processing parameters used in Metashape (2.2.2) and WebODM (2.9.2)

As expected, the flights conducted under low-light conditions (pre-dawn and post-sunset) exhibited alignment challenges, due to the reduced textural detail in the images, an issue well documented in photogrammetric literature (Ciccone, 2021). This limitation particularly affected Metashape, which struggled to detect sufficient tie points. In contrast, WebODM demonstrated greater robustness in processing low-light datasets, successfully generating orthomosaics for the same flights. Midday datasets, by comparison, were processed without difficulty by both software packages. The only notable difference concerned the extent of the final orthomosaic: WebODM tended to truncate the peripheral areas of the flight grid, failing to process the outermost image set (Fig. 2).

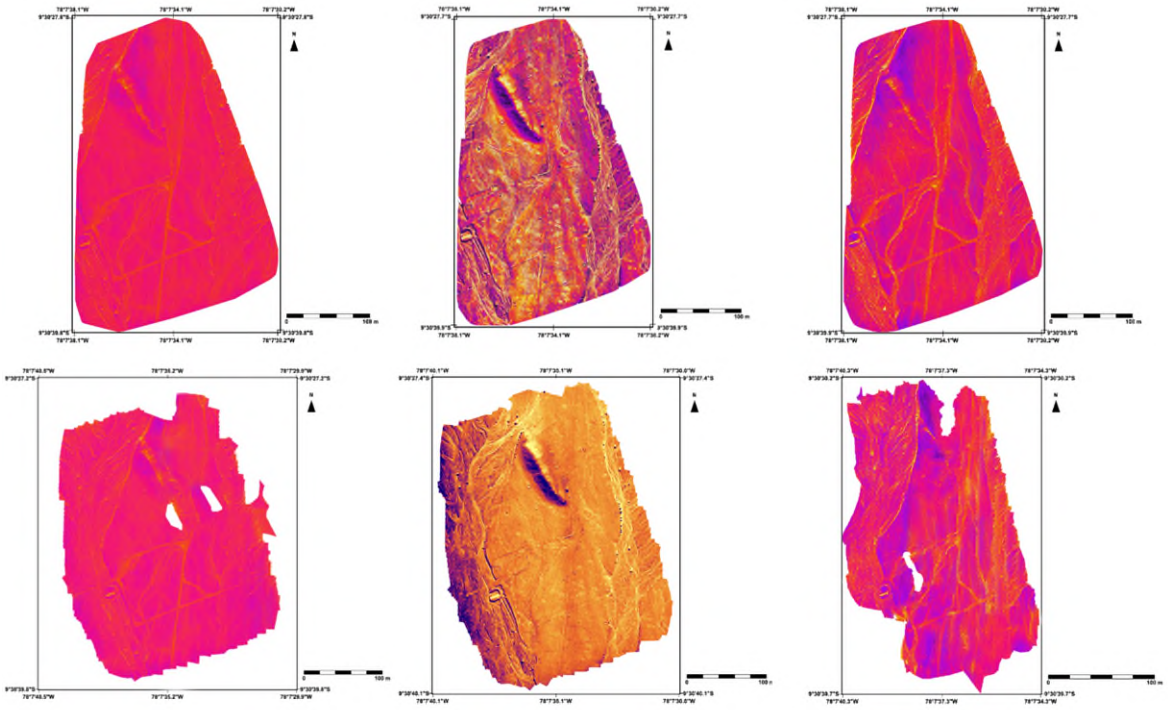


**Fig.2** Comparison of thermal orthomosaic reconstruction. Comparison between WebODM (top) and Metashape (bottom) orthomosaics from the pre-dawn (left), midday (center), and post-sunset (right) thermal datasets, highlighting differences in edge truncation and mosaic extent.

The resulting orthomosaics were then compared to identify linear or geometric patterns indicative of potential subsurface or surface anomalies corresponding to known or suspected geoglyph locations. The analysis first focused on thermal maps, aiming to determine which time of day provided the greatest contrast. Results were subsequently cross-compared with RGB imagery to evaluate the relative performance of thermal sensing.

Initially, comparisons were made using the raw orthomosaics, enhanced only through adaptive histogram equalization (Fig. 3).

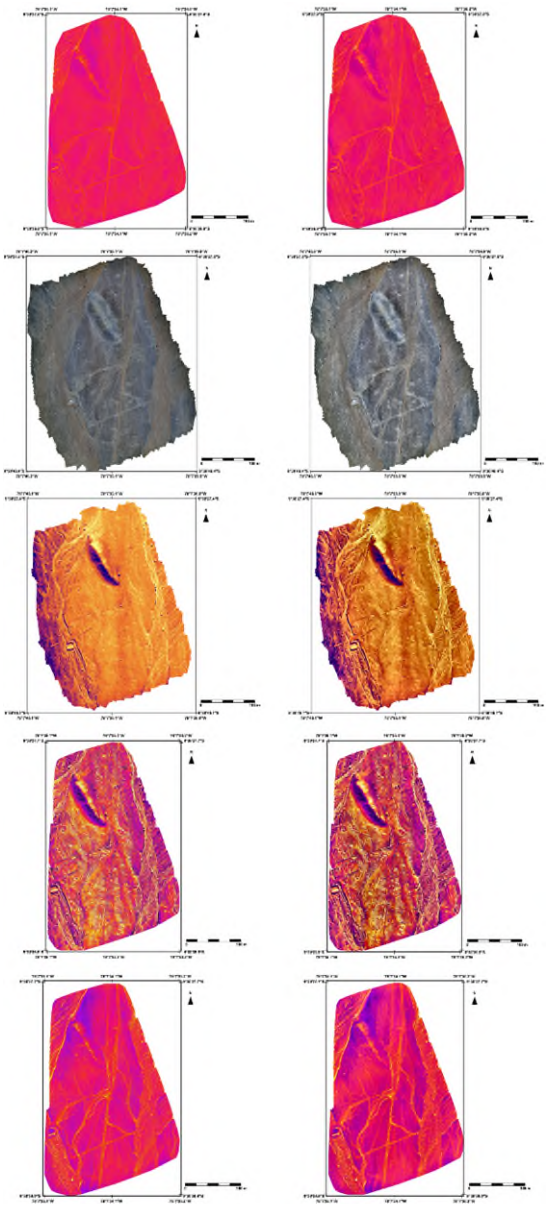


**Fig. 3** Effect of adaptive histogram equalization on orthomosaic visualization. Comparison between the original orthomosaics (left) and those enhanced by adaptive histogram equalization (right), illustrating the improved visibility of linear and geometric archaeological anomalies. From top to bottom: pre-dawn, midday RGB, midday Metashape, midday WebODM, post-sunset.
.

A second analytical phase concentrated on a selected area of interest measuring approximately 2.15 ha (Fig. 4), encompassing a well-documented pre-Hispanic roadway about 6 m wide and 860 m long (Pineda Quevedo, 2020, fig. 4, D7).

Within this sector, the following features were identified and were used as a benchmark for assessing the effectiveness of the processes implemented:

(a) a large negative geoglyph (ca. 50 × 25 m), rectangular in plan, created by material removal and accumulation along its borders;

(b) a positive spiral geoglyph about 8 m in diameter;

(c) several linear negative traces, possibly representing linear geoglyphs;

(d) modern trackways, partially overlapping ancient features;

(e) a small rectangular negative trace (ca. 6 × 4 m) of uncertain interpretation, adjacent to the large rectangular geoglyph;

(f) a modern boundary line crossing the ancient pathway and the rectangular geoglyph.

(g) a series of pseudo-circular traces arranged in a notably regular pattern, spaced approximately 8 m apart, and aligned along SE–NW oriented lines that are themselves separated by roughly 40 m.

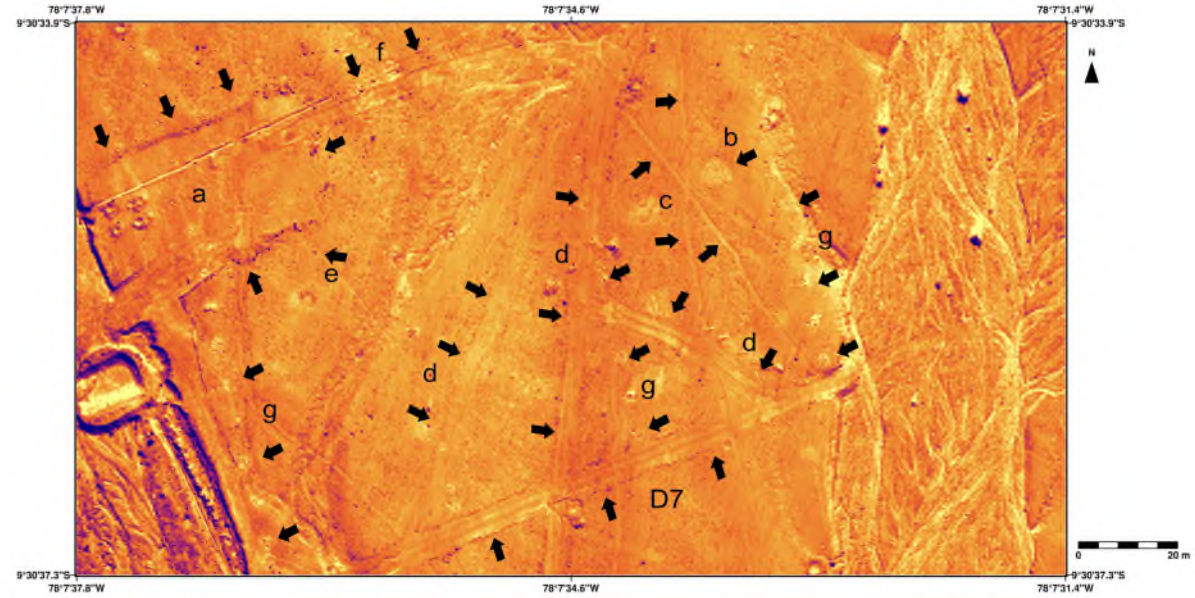



**Fig.4**. Area of interest and mapped archaeological features. Selected 2.15-ha area of interest showing the principal archaeological and modern features, including the negative rectangular geoglyph (a), positive spiral geoglyph (b), linear negative traces (c), modern trackways (d), small rectangular trace (e), field boundary (f), regularly spaced pseudo-circular traces (g), and the pre-Hispanic roadway (D7).

All images of this selected area, across the three sensors and three thermal time intervals, were subsequently processed using multiple interpolation and enhancement methods, designed to emphasize subtle patterns related to geoglyph morphology. The analyses were conducted using the open-source tool S.A.D.A. (Ciccone et al. 2026), developed by the National Research Council – Institute of Cultural Heritage Sciences (CNR – ISPC) as part of the PNRR (National Recovery and Resilience Plan) CHANGES project.

### 2.4. Data Post-processing

The post-processing operations were divided into three methodological categories (Table 2; Fig. 5): radiometric interpolation, Raster interpolation, LISA.

| Interpolation | | Pre-Dawn Thermal | Midday Thermal WebODM | Midday Thermal Metashape | Midday RGB | Post-sunset Thermal |
|---|---|---|---|---|---|---|
| Radiometric interpolation | Metashape | | | X | | |
| | Thermal Image Analysis | X | X | | | X |
| Raster interpolation in S.A.D.A. | Histogram Equalization | X | X | X | X | X |
| | Histogram Adaptive Equalization | X | X | X | X | X |
| | Histogram logarithmic transformation | X | X | X | X | X |
| | | | | | | |

| | | | | | | |
|---|---|---|---|---|---|---|
| LISA | Moran's I | X | X | X | X | X |
| | Getis-Ord G | X | X | X | X | X |

**Tab. 2** Overview of radiometric and raster-based interpolations applied to thermal and RGB datasets across the three thermal acquisition times, indicating which methods were applied to each dataset (Metashape or Thermal Image Analysis radiometric rescaling, histogram transformation and LISA)

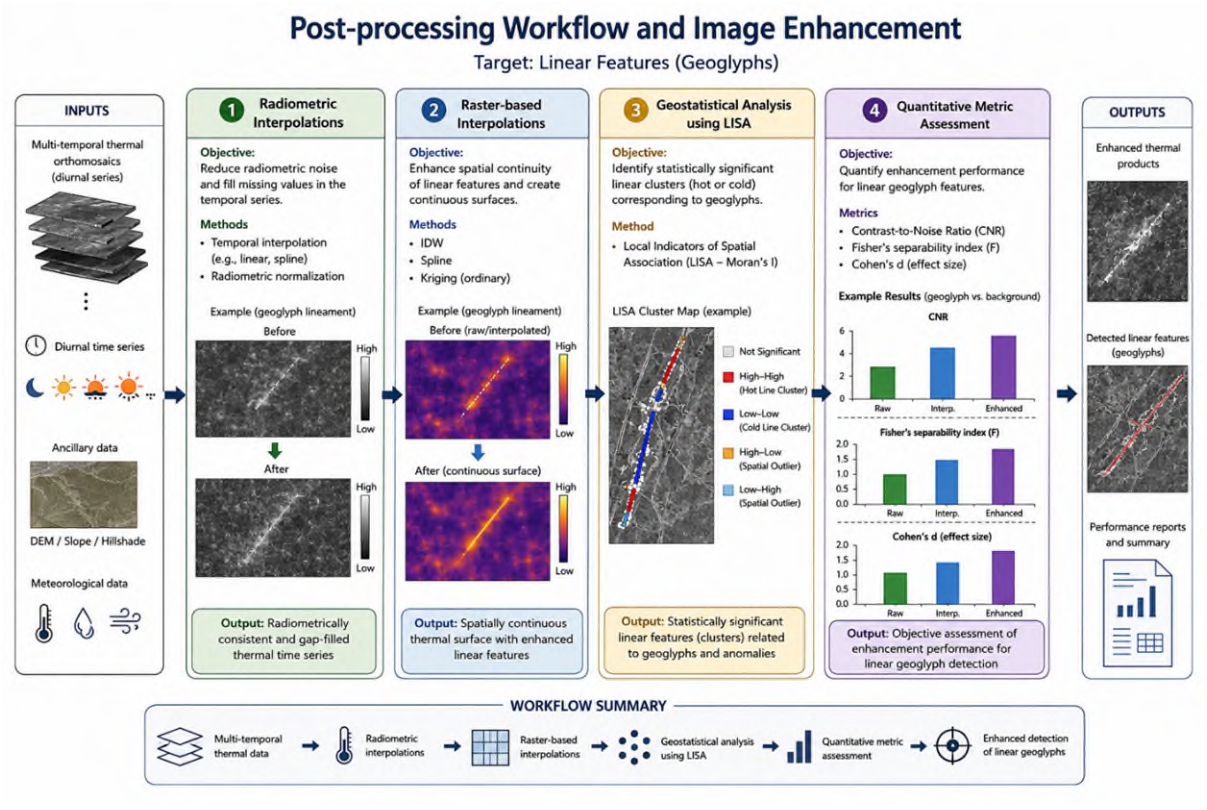



**Fig. 5.** Post-processing workflow adopted for the enhancement and quantitative assessment of linear archaeological features in multi-temporal thermal imagery. The workflow integrates radiometric interpolation, raster-based enhancement, local spatial-statistical analysis using Local Moran's I and the Getis–Ord statistic, and ROI-based separability metrics, including the contrast-to-noise ratio, Fisher's separability criterion, and Cohen's d. The outputs consist of enhanced thermal products, statistically significant spatial clusters, detected linear features, and comparative performance summaries.

The analyses included radiometric interpolations exploiting the absolute temperature values contained in the R-JPEG imagery, raster-based transformations based on histogram adjustments, and local spatial-statistical analyses using Local Moran's I and the Getis–Ord statistic.

Radiometric interpolations were performed directly within Metashape which allow dynamic rescaling of the thermal range based on user-defined temperature limits around the mean value. For detailed analyses within the area of interest, we employed the open-source software Thermal Image Analysis (Detect Technologies Pvt. Ltd.), which enables ROI-based scaling—that is, recalibrating visualization and temperature range according to the mean values measured within a specific region of interest (Fig. 5).

Raster-based interpolations (Abate 2021) and LISA indices (Getis, Ord, 1992; Anselin, 1995; Ord, Getis, 1995; Lasaponara, Masini, 2018) were conducted within S.A.D.A. In this phase, all images from the selected area were first subjected to a basic interpolation using equalization, adaptive equalization, and logarithmic transformation of the histogram, aimed at enhancing local contrast and improving the visual distinction of subtle surface variations. LISA are a set of geospatial statistical methods used to identify and measure local spatial patterns and spatial clustering within a dataset. Unlike global spatial statistics, which provide a single measure of overall spatial autocorrelation, LISA evaluates whether each individual location exhibits a significant relationship with its neighbouring locations. The most widely used LISA method is the Local Moran's I statistic, and the Getis–Ord G

index. Local Moran's I quantifies whether a spatial unit has values similar to or different from those of its surrounding neighbours. The Getis–Ord G index provides a different perspective by focusing specifically on the concentration of high or low values within a defined spatial neighbourhood. In the context of remote sensing and archaeological investigations, Local Moran's I is particularly useful because it enables the spatial discrimination of coherent anomalies from background variability. For example, persistent thermal anomalies associated with buried archaeological structures may appear as statistically significant High–High clusters, indicating areas where elevated thermal responses are spatially organized rather than randomly distributed. Conversely, isolated anomalous pixels may be classified as spatial outliers and treated differently during interpretation. Getis–Ord G focuses on identifying statistically significant concentrations of high or low values (hot spots and cold spots). Compared with the Getis–Ord G index, Local Moran's I provides a more detailed characterization of spatial relationships and it is more informative when the objective is to understand the spatial structure and morphology of detected features, whereas Getis–Ord G is more suitable for highlighting areas of concentrated intensity. In archaeological remote sensing, the two approaches are complementary: Getis–Ord G identifies significant zones of thermal or spectral accumulation, while Local Moran's I provides a finer interpretation of their internal spatial organization and potential archaeological relevance.

Results from the area investigated in this study are shown in Fig. 6.

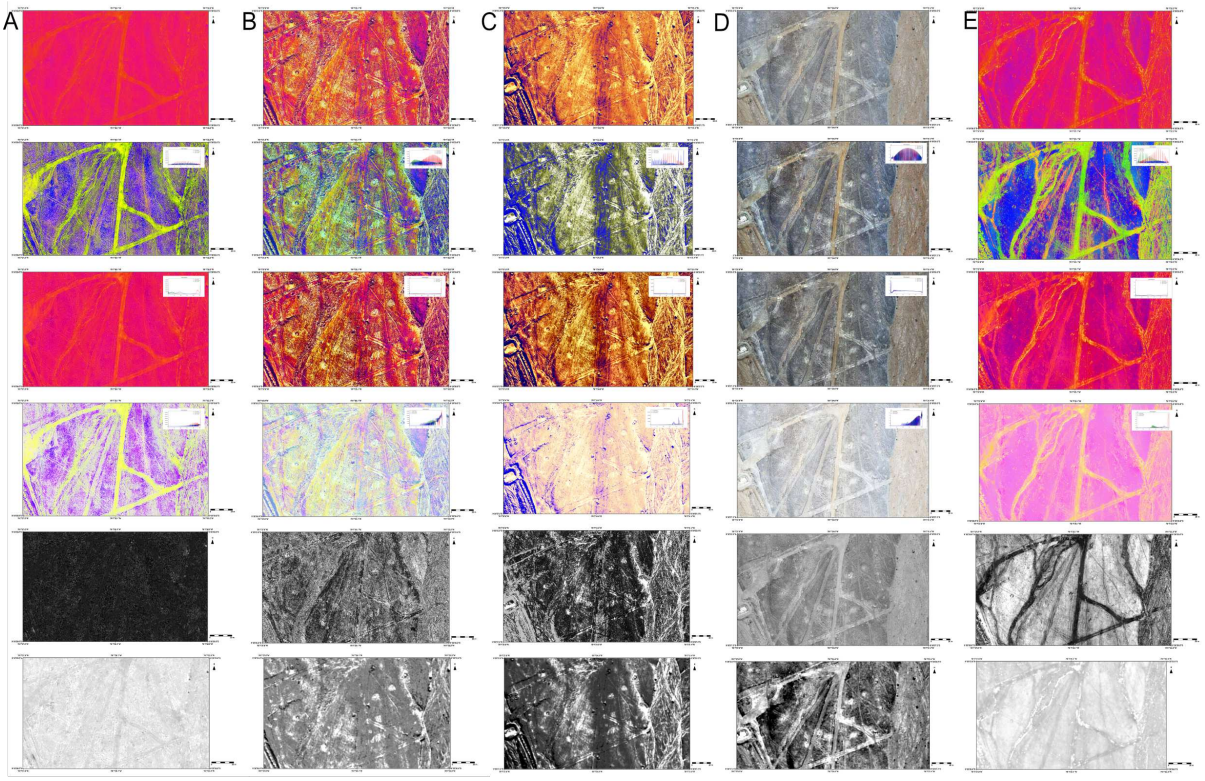



**Fig. 6** Comparison of enhancement methods across acquisition times**.** Multi-temporal comparison of data: A) pre-dawn, B) midday WebODM, C) midday Metashape, D) midday RGB, E) post-sunset. From top to bottom in column: raw data, histogram-equalized, adaptive histogram-equalized, log-transformed. LISA Moran's I, LISA Getis-Ord G.

### 2.5 Quantitative metric assessment

Finally, to objectively evaluate the impact of the different radiometric and raster-based processing techniques, a quantitative metric assessment was conducted on all five images (pre-dawn thermal, midday thermal processed in WebODM, midday thermal processed in Metashape, midday RGB, and post-sunset thermal). Within the selected 2.15-ha area of interest, two classes of Regions of Interest (ROIs) were manually defined: (i) anomaly ROIs corresponding to well-documented geoglyph features (positive and negative), and (ii) background ROIs representing undisturbed surrounding terrain with comparable surface characteristics. The same ROIs were applied consistently across all datasets and post-processing outputs to ensure comparability (Fig. 7).

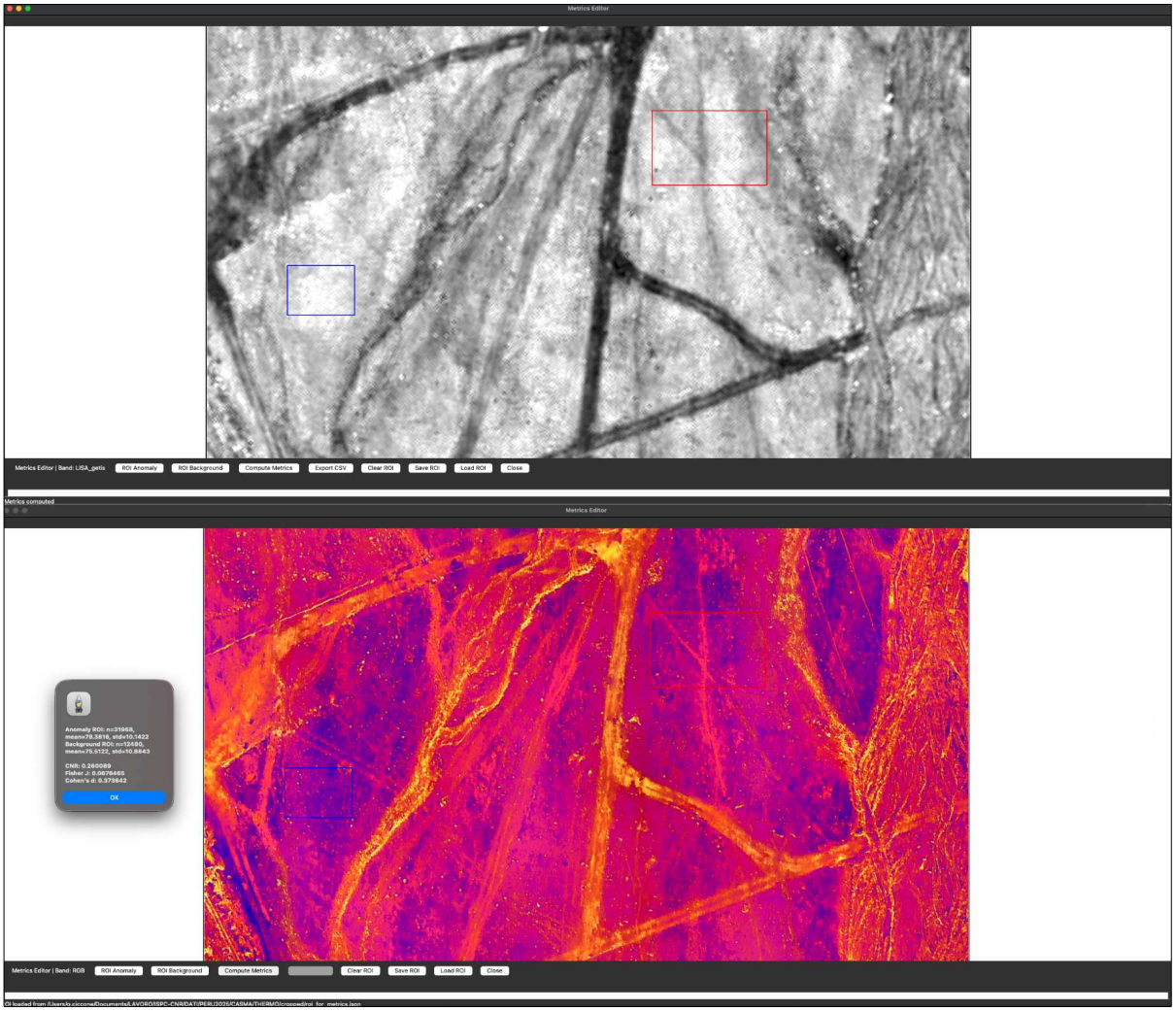



**Fig. 7** ROI-based quantitative metric assessment**.** Examples of metric analyses performed on the post-sunset image. The upper panel shows Moran's I; the lower panel shows adaptive histogram equalization. In both images, the ROIs used for the analysis are visible: anomaly ROIs are highlighted in red, and background ROIs in blue. In the lower image, the results of the metric computations performed in S.A.D.A. are also displayed.

For each image version (raw, histogram equalized, adaptive histogram equalized, logarithmic transform, LISA Moran's I, and LISA Getis-Ord G), descriptive statistics (mean and standard deviation) were extracted from both anomaly and background ROIs. Three complementary separability metrics were then computed:
(1) the Contrast-to-Noise Ratio (CNR), expressing the difference between anomaly and background means normalized by their combined variability (Welvaert and Rosseel 2013; Timischl 2015):

$$\mathrm{CNR} = \frac{|\mu_a - \mu_b|}{\sqrt{\sigma_a^2 + \sigma_b^2}} \qquad (1)$$

(2) Fisher's separability index (J), quantifying class discrimination strength (Fisher 1936; Duda, Hart, and Stork 2000):

:

$$J = \frac{(\mu_a - \mu_b)^2}{\sigma_a^2 + \sigma_b^2} \qquad (2)$$

(3) Cohen's d, representing the standardized effect size between the two ROI distributions (Cohen 1988; Lakens 2013):

(3)

These metrics allowed a reproducible and sensor-independent comparison of enhancement performance across acquisition times and processing workflows.

## 3. Results

Radiometric processing shows that reassigning the thermal color scale to a narrower, locally recalibrated temperature range—centered on the mean temperature—substantially improves contrast and the readability of subtle surface anomalies within the area of interest (Figure 8).

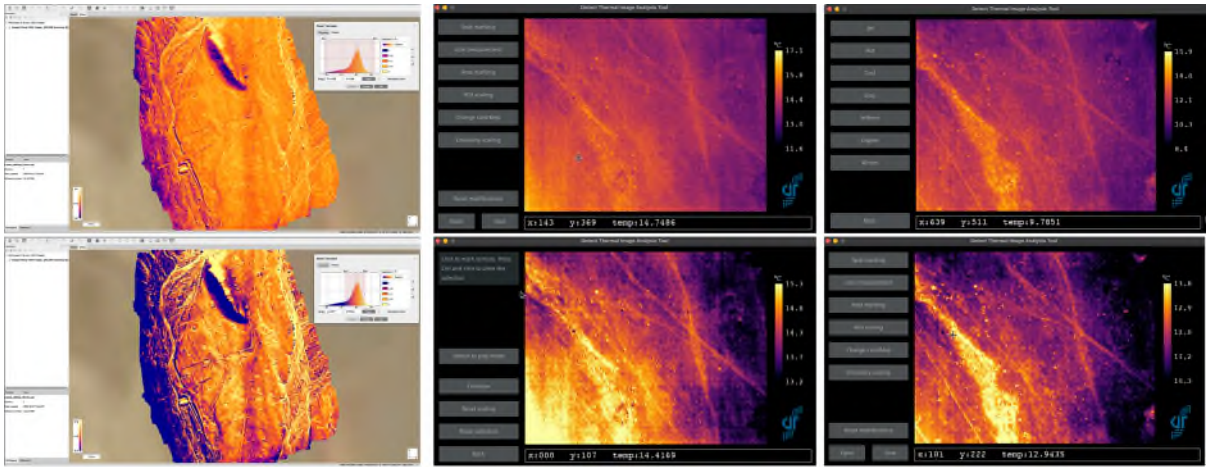


**Fig. 8** Radiometric recalibration of thermal orthomosaics (midday in Metashape; pre-dawn and post-sunset in Thermal Image Analysis), illustrating improved visibility of spiral and linear geoglyphs after narrowing temperature ranges around mean values.

For the midday thermal orthomosaic processed in Agisoft Metashape, the radiometric adjustment refined the original thermal range from 24.1–41.1 °C to a much narrower interval of 31.3–37.8 °C, resulting in a clear improvement in the legibility of all detectable anomalies, including spiral and linear geoglyphs. This demonstrates that, even under conditions of maximum solar irradiance, contrast can be recovered when the thermal dynamic range is optimized around the temperature distribution of the target landscape.

For the pre-dawn flight, radiometric enhancement focused specifically on the area containing the spiral geoglyph. In this case, narrowing the thermal scale from 11.7–17.1 °C to 13.2–15.3 °C substantially increased the readability of both the spiral geoglyph and the associated linear traces.

The same area was also examined in the radiometric analysis of the post-sunset thermal flight. In this case, the processing required a recalibration of the thermal scale, narrowing the original range of 8.4–15.9 °C to a more restricted interval of 10.3–13.8 °C. This adjustment enhanced the overall contrast of the traces, making the linear features in particular more readable. However, despite the improved contrast, the spiral geoglyph did not emerge with sufficient clarity to be reliably distinguished without reference to the images acquired at other times of day. The recalibration therefore improved legibility only partially, confirming that this specific geoglyph is not effectively detectable in the post-sunset dataset alone.

It is important to note, however, that recalibrating the color scale around a restricted temperature interval inevitably produces side effects: areas originally characterised by higher temperatures become saturated ("burned"), while those with lower values tend to darken, resulting in a loss of detail at the extremes of the thermal distribution. Consequently, if the analytical aim is to enhance detail specifically in hotter or cooler zones, the thermal range must be recalibrated accordingly around those subsets of values.

Regarding the raster-based processing performed in S.A.D.A., the application of several automatic histogram modification algorithms reveals a differentiated performance. Across all five analyzed images, both global histogram equalization and adaptive histogram equalization consistently outperform the logarithmic transformation. From a qualitative perspective, anomalies appear more clearly detectable when the first two histogram enhancement techniques are applied. This trend is particularly evident in the four thermal datasets, where contrast between anomalies and background is noticeably improved after equalization. In contrast, for the midday RGB image, histogram enhancement produces only limited variation, and the differences among the tested methods do not substantially alter anomaly visibility.

From a qualitative perspective, Local Moran's I generally preserves the morphology of archaeological anomalies more effectively than the Getis–Ord statistic. However, this pattern is not uniformly reflected in the quantitative metrics, in which Getis–Ord frequently produces higher anomaly–background separability values. Daylight LISA outputs generally provide the clearest morphological representation of the investigated features. In the pre-dawn dataset, several anomalies become difficult to recognize visually, despite the relatively high ROI-based separability values returned by the local spatial statistics. In the post-sunset dataset, these methods effectively highlight negative linear anomalies but do not clearly recover the morphology of the positive spiral geoglyph. This indicates that the effectiveness of spatial-statistical enhancement depends both on anomaly type and on the thermal phase represented by the acquisition.

The comparative analysis of all flight datasets reveals the following trends regarding the visibility and detectability of the investigated anomalies, from a qualitative point of view:

- The negative rectangular geoglyph (a) is generally observable in all images, with the clearest definition appearing in the midday thermal orthomosaic processed with Metashape.

- The positive spiral geoglyph (b) is visible in the pre-dawn and midday thermal datasets, as well as in the midday RGB orthophoto. However, its morphology is less clearly defined in the pre-dawn Local Moran's I output. In contrast, in the post-sunset thermal dataset, the geoglyph is not clearly recognizable in the unprocessed orthomosaic, the globally histogram-equalized image, or the logarithmically transformed version. Only a very faint indication of the spiral is visible after adaptive histogram equalization and in the Local Moran's I output. It should be noted that, without confirmation from the other flight datasets, the geoglyph would not have been identifiable in this case (Fig.9).

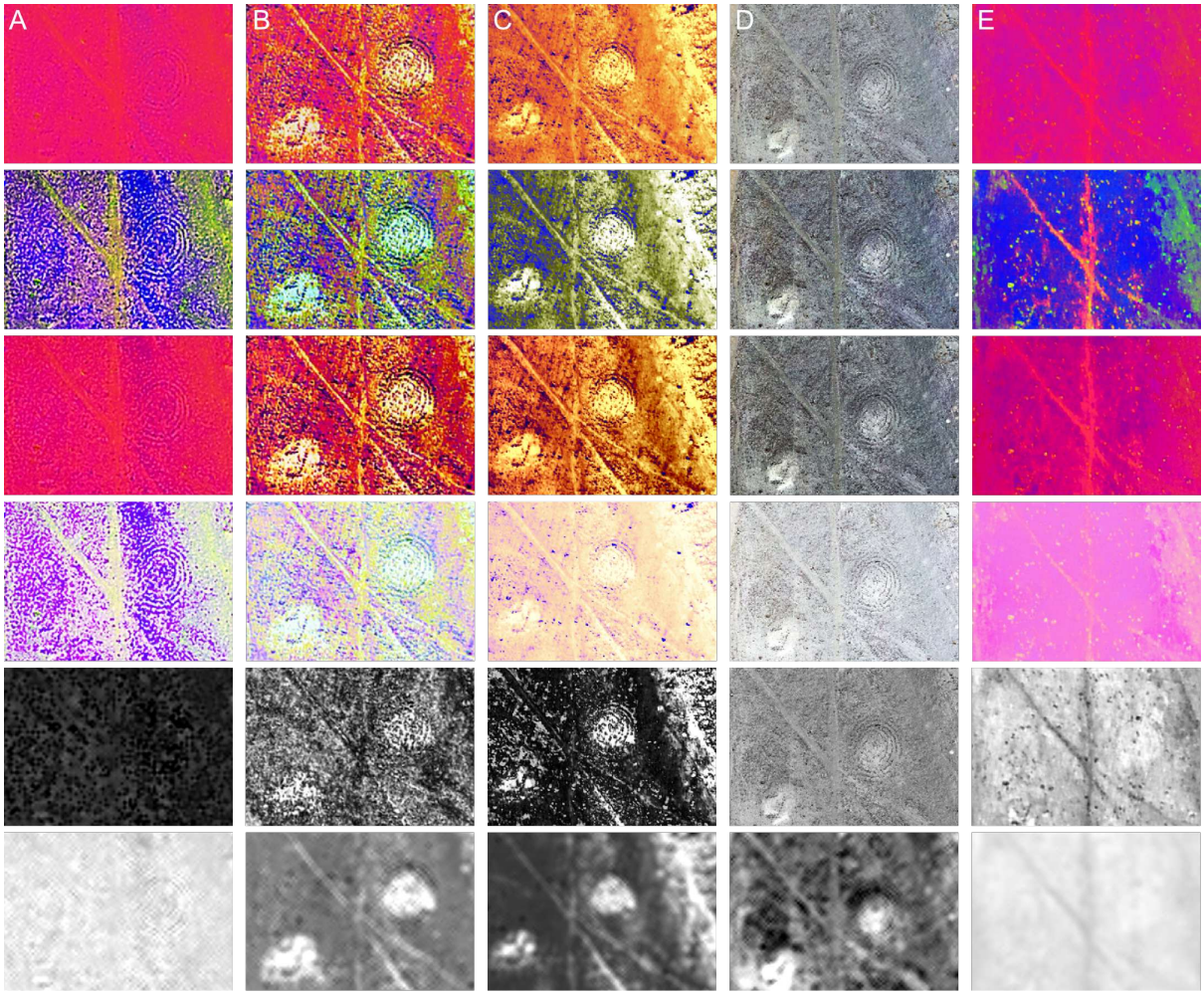



**Fig. 9** Multi-temporal visibility of the spiral geoglyph. Visibility of the spiral positive geoglyph across acquisition times and enhanced images. A) pre-dawn, B) midday WebODM, C) midday Metashape, D) midday RGB, E) post-sunset. From top to bottom in column: raw data, histogram equalized image, LISA Moran's I, LISA Getis-Ord G. histogram-equalized images, histogram adaptive equalized image, and histogram log transformed image.

- The possible linear geoglyphs (c) are fairly visible in all images examined. They are most clearly expressed in the midday thermal imagery, particularly in the unprocessed orthomosaics, the histogram-enhanced versions, and the Local Moran's I outputs derived from the midday and post-sunset datasets. By contrast, their morphological detail is less clearly preserved in the pre-dawn local-statistics outputs.
- The traces of modern pathways (d), the field boundary (f), and the pre-Hispanic D7 pathway are observable in all images, both in the unprocessed versions and in all post-processed outputs.
- The small negative rectangular trace (e) is clearly visible in the raw midday thermal orthomosaics and in the histogram-enhanced products, but it is not preserved in the corresponding Getis–Ord output. In the pre-dawn thermal orthomosaic, the feature is still detectable, though with reduced clarity. In the post-sunset thermal dataset, it disappears entirely and does not appear in any of the processed or unprocessed images.
- The regularly arranged pseudo-circular traces (g) are clearly visible in the midday RGB orthophoto and are further emphasized in both the histogram-enhanced and local spatial-statistics outputs. They are only partially visible in the midday thermal images, though far less distinctly than in the visible band, and they disappear completely in the pre-dawn and post-sunset thermal datasets, where they are not observable in any of the resulting images.

The quantitative metrics reveal marked variation in anomaly–background separability across acquisition times and processing methods (Table 3). Raw orthomosaics generally exhibit low to moderate separability, with CNR values ranging from approximately 0.29 to 0.52. This indicates that differences between anomaly and background values are frequently small relative to their combined variability in the unprocessed datasets. Global histogram equalization produces dataset-dependent results: it substantially improves separability in the pre-dawn dataset, produces only modest gains in some thermal datasets, and reduces separability in others. Adaptive histogram equalization consistently lowers CNR values relative to the corresponding raw images, probably because the amplification of local contrast also increases within-class variability.

Local spatial-statistical processing produces the highest separability values in each of the main acquisition datasets, although the best-performing statistic varies among datasets. Getis–Ord produces the strongest enhancement in the pre-dawn and post-sunset thermal datasets, with the post-sunset Getis–Ord output recording the highest CNR and Fisher J values in the study. In the midday RGB dataset, Local Moran's I produces the largest increase in anomaly–background separability. These results show that local spatial analysis can improve numerical anomaly discrimination in both thermal and visible-spectrum imagery, although high separability values do not necessarily correspond to equally clear morphological interpretability.

The midday thermal orthomosaic generated with Metashape generally exhibits higher anomaly–background separability than its WebODM counterpart in the raw image and in most enhanced products. The only exception is the Local Moran's I output, for which the WebODM product yields a higher CNR value. These differences suggest that the quality and radiometric characteristics of the photogrammetric reconstruction can influence the performance of subsequent analytical procedures. Overall, the quantitative results show that local spatial-statistical methods often produce larger increases in anomaly–background separability than radiometric or histogram-based contrast transformations. This advantage is particularly evident in the pre-dawn and post-sunset thermal datasets, although it is not uniform across all statistics and processing conditions. Moreover, higher ROI-based separability does not necessarily correspond to clearer morphological interpretability of individual archaeological features.

| | ROI Anomaly n | Mean | Std | ROI background n | Mean | Std | CNR | Fisher_J | Coehns_d |
|---|---|---|---|---|---|---|---|---|---|
| **PRE-DAWN** | 31968 | 98.5076 | 5.99439 | 12480 | 96.1251 | 5.4864 | 0.293191 | 0.0859612 | 0.406833 |
| **PRE-DAWN_equalize** | 31968 | 109.926 | 47.4457 | 12480 | 81.0243 | 41.4803 | 0.458598 | 0.210312 | 0.63036 |
| **PRE-DAWN _adapt_equalize** | 31968 | 94.0785 | 13.926 | 12480 | 90.7862 | 13.2104 | 0.17152 | 0.0294191 | 0.239811 |
| **PRE-DAWN log_transform** | 31968 | 162.505 | 37.6612 | 12480 | 146.25 | 38.013 | 0.303777 | 0.0922807 | 0.430484 |
| **PRE-DAWN LISA_Moran** | 31968 | 35.4628 | 16.242 | 12480 | 49.8286 | 11.1468 | 0.729263 | 0.531824 | -0.958529 |
| **PRE-DAWN _LISA_getis** | 31968 | 238.197 | 10.737 | 12480 | 247.784 | 6.16021 | 0.7745 | 0.59985 | -0.991122 |
| | | | | | | | | | |
| **MIDDAY_ODM** | 31968 | 122.597 | 44.9417 | 12480 | 142.412 | 44.8896 | 0.311933 | 0.0973023 | -0.441028 |
| **MIDDAY_ODM_equalize** | 31968 | 126.263 | 53.7014 | 12480 | 50.751 | 50.9702 | 0.330747 | 0.109393 | -0.462488 |
| **MIDDAY_ODM_adapt_equalize** | 31968 | 115.779 | 68.0077 | 12480 | 125.551 | 63.7938 | 0.104806 | 0.0109844 | -0.146186 |
| **MIDDAY_log_transform** | 31968 | 184.016 | 63.1754 | 12480 | 194.736 | 50.1603 | 0.13289 | 0.0176596 | -0.179238 |
| **MIDDAY_ODM_LISA_moran** | 31968 | 108.592 | 54.857 | 12480 | 87.9923 | 50.2205 | 0.276979 | 0.0767172 | 0.384356 |
| **MIDDAY_ODM_LISA_getis** | 31968 | 143.776 | 36.5049 | 12480 | 160.81 | 30.3924 | 0.358613 | 0.128604 | -0.488132 |
| | | | | | | | | | |
| **MIDDAY_PSX_temp_modif** | 31968 | 159.961 | 41.6206 | 12480 | 125.93 | 50.5224 | 0.519887 | 0.270283 | 0.768176 |
| **MIDDAY_PSX_temp_modif_equalize** | 31968 | 147.448 | 61.2935 | 12480 | 106.364 | 59.6884 | 0.480212 | 0.230603 | 0.675206 |

| | | | | | | | | | |
|---|---|---|---|---|---|---|---|---|---|
| **MIDDAY_PSX_temp_modif_adapt_equalize** | 31968 | 132.041 | 69.8104 | 12480 | 90.8698 | 69.1411 | 0.419027 | 0.175583 | 0.591346 |
| **MIDDAY_PSX_temp_modif_log_transform** | 31968 | 204.474 | 50.7441 | 12480 | 159.645 | 75.7015 | 0.491889 | 0.241954 | 0.761998 |
| **MIDDAY_PSX_temp_modif_LISA_moran** | 31968 | 72.3997 | 70.8455 | 12480 | 91.8682 | 74.6141 | 0.189216 | 0.035802 | -0.270682 |
| **MIDDAY_PSX_temp_modif_LISA_getis** | 31968 | 153.518 | 41.8077 | 12480 | 114.234 | 44.1315 | 0.646215 | 0.417594 | 0.92491 |
| | | | | | | | | | |
| **MIDDAY_RGB** | 31968 | 152.776 | 52.3967 | 12480 | 128.157 | 64.3735 | 0.296605 | 0.087974 | 0.439476 |
| **MIDDAY_RGB_equalize** | 31968 | 119.503 | 32.962 | 12480 | 106.647 | 42.7774 | 0.238056 | 0.056670 | 0.357217 |
| **MIDDAY_RGB_adapt_equalize** | 31968 | 115.43 | 32.395 | 12480 | 108.955 | 38.462 | 0.128752 | 0.016577 | 0.189274 |
| **MIDDAY_RGB_log_transform** | 31968 | 204.133 | 19.6552 | 12480 | 199.316 | 24.2796 | 0.154207 | 0.023779 | 0.228775 |
| **MIDDAY_RGB_LISA_moran** | 31968 | 72.4058 | 48.7568 | 12480 | 46.854 | 73.5923 | 0.843336 | 0.711215 | -1.30987 |
| **MIDDAY_RGB_LISA_getis** | 31968 | 107.589 | 40.4448 | 12480 | 73.976 | 70.2324 | 0.414728 | 0.171999 | 0.664128 |
| | | | | | | | | | |
| **POST-SUNSET** | 31968 | 91.0682 | 4.43587 | 12480 | 88.3699 | 5.82519 | 0.36852 | 0.135807 | 0.554494 |
| **POST-SUNSET_equalize** | 31968 | 76.2762 | 32.9574 | 12480 | 59.4001 | 25.728 | 0.403634 | 0.16292 | 0.54268 |
| **POST-SUNSET_adapt_equalize** | 31968 | 79.3816 | 10.1422 | 12480 | 75.5122 | 10.8843 | 0.260089 | 0.067646 | 0.373642 |
| **POST-SUNSET_log_transform** | 31968 | 174.335 | 8.62672 | 12480 | 173.287 | 7.4996 | 0.091672 | 0.008403 | 0.125862 |
| **POST-SUNSET_LISA_moran** | 31968 | 94.418 | 30.9196 | 12480 | 228.665 | 29.2347 | 0.804804 | 0.647709 | -1.12445 |
| **POST-SUNSET_LISA_getis** | 31968 | 238.439 | 5.88692 | 12480 | 245.674 | 5.08283 | 0.930224 | 0.865316 | -1.27539 |

**Tab. 3** Overview of quantitative metrics results.

## 4. Discussion

A first result emerging from this study concerns the differences in output between the two photogrammetric software packages used—Metashape and WebODM—despite processing the same thermal datasets. The contrast between the two is particularly significant: while Metashape provides superior results for the midday flight, it encounters markedly greater difficulties than WebODM when processing images acquired before sunrise and after sunset, in conditions of reduced illumination and lower thermal intensity.

The midday orthomosaic generated in Metashape shows higher definition and lower noise, producing a markedly cleaner image than the orthomosaic generated from the same dataset in WebODM. This has a direct impact on all subsequent post-processing steps, confirming that Metashape yields higher-quality analytical results for the midday flight. Conversely, in the flights conducted before dawn and after sunset, Metashape struggles to align the images correctly, resulting in gaps and pronounced distortions in the orthomosaic. These issues make it impossible to perform a reliable interpretation of the anomalies and render further post-processing useless. It is also worth noting that Metashape's ability to perform radiometric processing internally allows for a first analytical interpretation directly within the software, an option theoretically available in WebODM, but which, in practice, could not be executed for any of the datasets used.

These observations indicate that photogrammetric software selection is not merely a technical consideration but may directly influence the interpretability of archaeological thermal datasets acquired under low-illumination conditions.

One of the most significant findings of this study is that midday thermal acquisitions consistently revealed all investigated archaeological anomalies, challenging the long-standing assumption that periods of reduced solar forcing invariably provide the optimal conditions for archaeological thermal prospection. Rather than being intrinsically unsuitable, daytime acquisitions can produce strong archaeological thermal contrasts when modern UAV-mounted sensors with high radiometric sensitivity are employed. In the present study, all anomalies were consistently detectable in the midday thermal orthomosaics generated by both Metashape and WebODM, although with slightly lower definition in the latter.

The contrasting behaviour of positive and negative geoglyphs demonstrates that archaeological thermal signatures depend not only on acquisition time but also on the interaction between construction technique, thermophysical properties, and the transient surface energy balance. Stone-built positive geoglyphs and excavated negative geoglyphs therefore follow distinct diurnal thermal trajectories, suggesting that different classes of archaeological features may require different acquisition strategies.

The positive spiral geoglyph (b), constructed by stone accumulation, was clearly visible in the pre-dawn and midday datasets but almost absent after sunset. This behaviour is explained by the different thermophysical properties of the stones relative to the surrounding soil. During the day, the stones attain higher temperatures because of their different volumetric heat capacity (Périsset & Tabbagh, 1981), whereas after sunset they cool rapidly, temporarily reducing thermal contrast. By pre-dawn, differential cooling restores sufficient contrast for the geoglyph to become detectable again.

Conversely, the negative linear (c) and rectangular (a) geoglyphs, created by removing surface material, expose a lighter substratum that absorbs and releases heat differently from the surrounding terrain. As a result, these features remain thermally distinct after sunset and continue to appear as slightly warmer anomalies before dawn, although with reduced contrast. The same thermal behaviour observed in both the pre-Hispanic D7 road and modern tracks indicates that thermal response is controlled primarily by material properties and surface structure rather than by the chronological age of the feature.

The behaviour of the small negative rectangular anomaly (e) differs markedly: it is clearly detectable in the midday thermal imagery, less visible in the pre-dawn flight, and completely absent in the post-sunset flight. This pattern is compatible with the interpretation that the anomaly is shallower, not reaching the deeper exposed substratum visible in the negative geoglyphs or in the repeatedly compacted surfaces of ancient and modern pathways. This shallower depth prevents the anomaly from following the same thermal evolution, suggesting a very recent origin, with no historical significance.

Finally, the visibility of the pseudo-circular anomalies arranged in a regular pattern (g) is of particular interest. These features are observable only in the midday flight, and far more clearly in the visible imagery than in the thermal data. This behaviour is consistent with an interpretation as modern surface disturbances, involving the accumulation of material of a different colour, more greyish than the yellow-reddish surrounding soil, thus easily detectable in RGB imagery but exhibiting thermal properties nearly identical to the surrounding terrain, resulting in no measurable thermal contrast.

About the metrics results, the quantitative separability analysis fundamentally strengthens the interpretative conclusions of this study by providing objective evidence for the differential performance of acquisition times and processing workflows. While visual inspection alone suggests improved anomaly visibility under certain conditions, the metric results demonstrate that these improvements are not uniformly attributable to simple contrast stretching. Instead, the most substantial gains derive from spatial autocorrelation analyses (LISA Moran and Getis-Ord), which enhance coherent local clusters rather than merely amplifying pixel-level intensity differences. The results also confirm that midday thermal data—particularly when processed in Metashape—provide consistently higher baseline separability than traditionally expected, challenging the long-held assumption that midday flights are diagnostically inferior. Furthermore, the strong performance of Getis-Ord G in pre-dawn and post-sunset datasets highlights the importance of spatial pattern reinforcement during phases of reduced global contrast. Importantly, the metric analysis demonstrates that adaptive histogram equalization, although visually appealing, can degrade statistical separability by increasing intra-class variance. By introducing reproducible quantitative metrics into the workflow, this study moves beyond qualitative interpretation and establishes a replicable framework for evaluating thermal survey effectiveness in arid archaeological contexts. Although the workflow is replicable, the observations derive from a single case study in a specific environmental setting characterized by coastal influences (e.g., morning humidity/fog and strong daytime evaporation). This underscores the importance of extending tests to different desert substrates, geomorphologies, and climatic regimes to determine the stability of the diurnal discrimination pattern.

Although the proposed methodological framework proved effective under the hyper-arid environmental conditions of the Casma Valley, its broader applicability should be evaluated in different archaeological and climatic settings. In particular, environments characterized by denser vegetation, greater soil moisture, or smaller diurnal temperature amplitudes may exhibit different thermal dynamics. Future comparative studies will therefore be essential to determine the generality of the diurnal patterns identified in this work.

## 5. Conclusion

The analyses conducted in the Casma Valley highlight two major considerations that deserve emphasis at the conclusion of this study.

First, the results confirm the crucial importance of conducting UAV thermal surveys at multiple times of day. Although this principle is widely acknowledged in the literature on archaeological thermal imaging, it is equally true that midday acquisitions have traditionally been regarded as of limited value (e.g., Casana et al., 2014, 2017; Hill et al., 2020), due to the strong solar irradiance that tends to mask subtle thermal differences.

The findings presented here (Ciccone, 2024), however, demonstrate that midday flights can in fact reveal the full range of surface anomalies, including both positive and negative geoglyphs, as well as modern and ancient pathways. Combined with other recent research, these results suggest that new generations of drone-mounted thermal sensors, with improved radiometric precision and the ability to fly at lower altitudes, are now capable of detecting very slight thermal contrasts even when solar radiation is at its peak. Consequently, excluding midday flights a priori can no longer be considered a valid methodological choice. Instead, midday imaging should be integrated as a standard component of any thermal survey aimed at identifying archaeological features.

Second, the study underscores the diagnostic potential of thermal imaging for differentiating between positive and negative geoglyphs, owing to the distinct thermal behaviors associated with their construction methods. In this case study, positive geoglyphs (formed by stone accumulation) and negative geoglyphs (created by surface removal) exhibited markedly different diurnal thermal cycles, leading to variable visibility across the three acquisition times. These differences appear structurally linked to material properties (e.g., volumetric heat capacity, emissivity, conductivity, and thermal inertia), indicating that thermal response can support typological interpretation and improve confidence in remote classification.

The integration of quantitative separability metrics further strengthens these conclusions by providing reproducible measures of anomaly–background contrast. The CNR, Fisher's separability criterion J, and Cohen's d collectively show that ROI-based anomaly–background separability varies across acquisition times and processing methods. Because the adopted Fisher criterion is mathematically equivalent to the squared CNR, the two measures describe the same underlying contrast on different scales. Post-sunset imagery produced the highest overall separability values, particularly after local spatial-statistical processing. However, the midday datasets showed heterogeneous performance: the Metashape thermal product achieved separability values comparable to those of the pre-dawn dataset, whereas the WebODM thermal product generally performed less well.

More importantly, the metric analysis reveals that the most substantial improvements in anomaly detectability derive not from simple radiometric contrast adjustments, but from spatial-statistical enhancement methods. Spatial autocorrelation analyses (LISA), particularly Moran's I and Getis-Ord G, produced higher separability values than histogram-based transformations, indicating that the reinforcement of coherent spatial clusters plays a decisive role in anomaly detection. These results confirm that the effectiveness of thermal prospection depends not only on acquisition timing, but also on the analytical strategy applied during post-processing.

By introducing reproducible quantitative metrics into the evaluation workflow, this study moves beyond qualitative assessment and establishes a replicable framework for comparing survey conditions and processing techniques. Such an approach enhances methodological transparency and provides a robust basis for optimizing future thermal drone campaigns in arid archaeological landscapes.

While these observations are based on a single case study in a highly specific environmental context, one characterized by marine humidity and coastal fog in the early morning, and intense evaporation during daytime hours, they nonetheless indicate a promising avenue for further research. Additional studies in different climatic and geomorphological settings are needed to determine whether these thermal distinctions are consistent across regions. Should these patterns be replicated elsewhere, the implications would be significant: thermal images alone could be used to distinguish geoglyph types, opening the way for reliable training datasets for deep-learning models aimed at large-scale, automated geoglyph detection.

Overall, the results clearly show that the systematic integration of drone-based thermal imaging, alongside conventional visible-spectrum surveys, has the potential to accelerate and enhance the detection of Peruvian geoglyphs, offering a powerful tool for both their documentation and protection. In a broader sense, the methodological framework presented here contributes to expanding remote-sensing strategies for archaeological

heritage, supporting the monitoring, safeguarding, and valorization of one of the most fragile cultural landscapes of the Andean region.

## References


Abate, N., Frisetti, A., Marazzi, F., Masini, N., & Lasaponara, R. (2021). Multitemporal–multispectral UAS surveys for archaeological research: The case study of San Vincenzo al Volturno (Molise, Italy). *Remote Sensing, 13*(14), Article 2719. https://doi.org/10.3390/rs13142719

Agapiou, A., Lysandrou, V., Lasaponara, R., Masini, N., & Hadjimitsis, D. G. (2016). Study of the variations of archaeological marks at Neolithic site of Lucera, Italy using high-resolution multispectral datasets. *Remote Sensing, 8*(9), Article 723. https://doi.org/10.3390/rs8090723

Agudo, P. U., Angás Pajas, J., Pérez-Cabello, F., Vicente Redón, J., & Ezquerra Lebrón, B. (2018). The potential of drones and sensors to enhance detection of archaeological cropmarks: A comparative study between multi-spectral and thermal imagery. *Drones, 2*(3), Article 29. https://doi.org/10.3390/drones2030029

Anselin, L. (1995). Local indicators of spatial association—LISA. *Geographical Analysis, 27*(2), 93–115.

Briones-M., L. (2006). The geoglyphs of the north Chilean desert: An archaeological and artistic perspective. Antiquity, 80(307), 9–24. https://doi.org/10.1017/S0003598X00093224

Burger, R. L. (1992). *Chavín and the origins of Andean civilization*. Thames and Hudson.

Casana, J., Kantner, J., Wiewel, A., & Cothren, J. (2014). Archaeological aerial thermography: A case study at the Chaco-era Blue J community, New Mexico. *Journal of Archaeological Science, 45*, 207–219. https://doi.org/10.1016/j.jas.2014.02.015

Casana, J., Wiewel, A., Cool, A., Hill, A., Fisher, K., & Laugier, E. (2017). Archaeological aerial thermography in theory and practice. *Advances in Archaeological Practice, 5*(4), 310–327. https://doi.org/10.1017/aap.2017.23

Ciccone, G. (2021). Un workflow open-source per l'elaborazione delle immagini termiche da drone. In J. Bogdani, R. Montalbano, & P. Rosati (Eds.), *ArcheoFOSS XIV 2020: Proceedings of the 14th International Conference, 15–17 October 2020* (pp. 35–43). Archaeopress.

Ciccone, G. (2024). Thermal analysis of evapotranspiration in cultivated fields for the detection of archaeological anomalies. *Archaeological Prospection*. Advance online publication. https://doi.org/10.1002/arp.1946

Ciccone, G., Abate, N., Frisetti, A., Amodio, A. M., Lasaponara, R., & Masini, N. (2026). Bridging the remote sensing gap in archaeology: The S.A.D.A. platform for accessible remote sensing images analysis. Journal of Cultural Heritage, 81, 20-35, https://doi.org/10.1016/j.culher.2026.06.026

Cohen, J. (1988). *Statistical power analysis for the behavioral sciences* (2nd ed.). Lawrence Erlbaum Associates.

Duda, R. O., Hart, P. E., & Stork, D. G. (2000). *Pattern classification* (2nd ed.). Wiley.

Fisher, R. A. (1936). The use of multiple measurements in taxonomic problems. *Annals of Eugenics, 7*(2), 179–188. https://doi.org/10.1111/j.1469-1809.1936.tb02137.x

Getis, A., & Ord, J. K. (1992). The analysis of spatial association by use of distance statistics. *Geographical Analysis, 24*(3), 189–206. https://doi.org/10.1111/j.1538-4632.1992.tb00261.x

Hill, A. C., Laugier, E. J., & Casana, J. (2020). Archaeological remote sensing using multi-temporal, drone-acquired thermal and near-infrared (NIR) imagery: A case study at the Enfield Shaker Village, New Hampshire. *Remote Sensing, 12*(4), Article 690. https://doi.org/10.3390/rs12040690

Hollesen, J., Jepsen, M. S., & Harmsen, H. (2023). The application of RGB, multispectral, and thermal imagery to document and monitor archaeological sites in the Arctic: A case study from South Greenland. *Drones, 7*(2), Article 115. https://doi.org/10.3390/drones7020115

James, K., Nichol, C. J., Wade, T., Cowley, D., Gibson Poole, S., Gray, A., & Gillespie, J. (2020). Thermal and multispectral remote sensing for the detection and analysis of archaeologically induced crop stress at a UK site. *Drones, 4*(4), Article 61. https://doi.org/10.3390/drones4040061

Klokočník, J., Kostelecký, J., & Pavelka, K. (2011). Google Earth: Inspiration and instrument for the study of ancient civilizations. *Geoinformatics FCE CTU, 6*, 193–211.

Lambers, K. (2006). The geoglyphs of Palpa, Peru: Documentation, analysis, and interpretation. Forschungen zur Archäologie Außereuropäischer Kulturen, Band 2. Bonn: Kommission für Archäologie

Außereuropäischer Kulturen, Deutsches Archäologisches Institut; Aichwald: Linden Soft. https://doi.org/10.34780/faak.v2i0.1000

Lakens, D. (2013). Calculating and reporting effect sizes to facilitate cumulative science: A practical primer for t-tests and ANOVAs. *Frontiers in Psychology, 4*, Article 863. https://doi.org/10.3389/fpsyg.2013.00863

Lasaponara, R., & Masini, N. (2007). Detection of archaeological crop marks by using satellite QuickBird multispectral imagery. *Journal of Archaeological Science, 34*(2), 214–221. https://doi.org/10.1016/j.jas.2006.04.014

Lasaponara, R., & Masini, N. (2018). Space-based identification of archaeological illegal excavations and a new automatic method for looting feature extraction in desert areas. *Surveys in Geophysics, 39*, 1323–1346. https://doi.org/10.1007/s10712-018-9480-4

Masini, N., Orefici, G., & Lancho Rojas, J. (2016). Nasca geoglyphs: Technical aspects and overview of studies and interpretations. In R. Lasaponara, N. Masini, & G. Orefici (Eds.), *The ancient Nasca world: New insights from science and archaeology* (pp. 217–238). Springer. https://doi.org/10.1007/978-3-319-47052-8_11

Masini, N., Orefici, G., Danese, M., Pecci, A., Scavone, M., & Lasaponara, R. (2016). Cahuachi and Pampa de Atarco: Towards greater comprehension of Nasca geoglyphs. In R. Lasaponara, N. Masini, & G. Orefici (Eds.), *The ancient Nasca world: New insights from science and archaeology* (p. 217-238). Springer, https://doi.org/10.1007/978-3-319-47052-8_11

Masini, N., & Lasaponara, R. (2020). Satellite and close-range analysis for the surveillance and knowledge improvement of the Nasca geoglyphs. *Remote Sensing of Environment, 236*, Article 111447, https://doi.org/10.1016/j.rse.2019.111447

Ord, J. K., & Getis, A. (1995). Local spatial autocorrelation statistics: Distributional issues and an application. Geographical Analysis, 27(4), 286–306. https://doi.org/10.1111/j.1538-4632.1995.tb00912.x

Pande-Chhetri, R., Abd-Elrahman, A., Liu, T., Morton, J., & Wilhelm, V. L. (2017). Object-based classification of wetland vegetation using very high-resolution unmanned air system imagery. European Journal of Remote Sensing, 50(1), 564–576. https://doi.org/10.1080/22797254.2017.1373602

Parcak, S. H. (2009). Satellite remote sensing for archaeology. Routledge. https://doi.org/10.4324/9780203881460

Pavelka, K., Šedina, J., & Matoušková, E. (2018). High resolution drone surveying of the Pista geoglyph in Palpa, Peru. Geosciences, 8(12), Article 479. https://doi.org/10.3390/geosciences8120479

Périsset, M. C., & Tabbagh, A. (1981). Interpretation of thermal prospection on bare soils. Archaeometry, 23(2), 169–187. https://doi.org/10.1111/j.1475-4754.1981.tb00304.x

Pineda Quevedo, J. (2020). Caminos y geoglifos en los valles de Casma y Sechín: Control y sacralidad. Arkinka.

Pozorski, T., Pozorski, S., & Rick, J. (1991). A bird geoglyph near Casma, Peru. Andean Past, 3, 187–192.

Pozorski, S., & Pozorski, T. (2011). La evolución del Periodo Inicial en el valle de Casma del Perú: Una historia de dos rivales políticos. In M. Giersz & I. Ghezzi (Eds.), Arqueología de la costa de Ancash. Institut Français d'Études Andines. https://doi.org/10.4000/books.ifea.7362

Sakai, M., Sakurai, A., Lu, S., Olano, J., Albrecht, C. M., Hamann, H. F., & Freitag, M. (2024). AI-accelerated Nazca survey nearly doubles the number of known figurative geoglyphs and sheds light on their purpose. Proceedings of the National Academy of Sciences of the United States of America, 121(40), e2407652121. https://doi.org/10.1073/pnas.2407652121

Sanchez Borjas, A. E., & Ghezzi, I. (2025). Estudio preliminar en la utilización de cámara térmica en el registro de geoglifos dañados en la costa norte del Perú. Práctica Arqueológica, 8(2), 64–81. https://doi.org/10.5281/zenodo.17879008

Scollar, I., Tabbagh, A., Hesse, A., & Herzog, I. (1990). Archaeological prospecting and remote sensing. Cambridge University Press.

Sever, T. L., & Wagner, D. W. (1991). Analysis of prehistoric roadways in Chaco Canyon using remotely sensed digital data. In C. D. Trombold (Ed.), Ancient road networks and settlement hierarchies in the New World (pp. 42–52). Cambridge University Press.

Sheets, P., & Sever, T. L. (1991). Prehistoric footpaths in Costa Rica: Transportation and communication in a tropical rainforest. In C. D. Trombold (Ed.), Ancient road networks and settlement hierarchies in the New World (pp. 53–65). Cambridge University Press.

Tello, J. C. (1956). Arqueología del valle de Casma: Culturas Chavín, Santa o Huaylas Yunga y Sub-Chimú. Informe de los trabajos de la Expedición Arqueológica al Marañón de 1937. Editorial San Marcos.

Timischl, F. (2015). The contrast-to-noise ratio for image quality evaluation in scanning electron microscopy. Scanning, 37(1), 54–62. https://doi.org/10.1002/sca.21179

Welvaert, M., & Rosseel, Y. (2013). On the definition of signal-to-noise ratio and contrast-to-noise ratio for fMRI data. PLoS ONE, 8(11), Article e77089. https://doi.org/10.1371/journal.pone.0077089

Wilson, D. J. (1989). Prehispanic settlement patterns in the Casma Valley, north coast of Peru: Preliminary results to date. Journal of the Steward Anthropological Society, 23(1–2), 189–227.

## Data availability

The datasets used and analysed during the current study are available from the corresponding author on reasonable request.

## Acknowledgements

The authors sincerely thank the **Unidad Ejecutora Chankillo, Ministerio de Cultura del Perú**, for facilitating access to the Chankillo Archaeological Complex and for its invaluable collaboration and support throughout the fieldwork. They also gratefully acknowledge all the personnel and collaborators involved in the UAV surveys, ground-truth data collection, data processing, and logistical assistance, whose contributions were essential to the successful completion of this research. The authors further thank the anonymous reviewers for their constructive comments and suggestions, which significantly improved the quality of this manuscript. This research was supported by: (1) the CHANGES Project, funded under the National Recovery and Resilience Plan (NRRP), Mission 4, Component 2, Investment Line 1.3 – Extended Partnerships (Spoke 5, Work Package 3), which supported the data processing activities; (2) the CNR-ISPC ITACA project, which supported the ground-truth data collection activities; and (3) the SHINE project (Strengthening of the National Hub of E-RIHS—European Research Infrastructure for Heritage Science), funded under PON Ricerca e Innovazione 2014–2020 (CCI: 2014IT16M2OP005), which supported the UAV-based data acquisition activities.

## Funding.

This research did not receive funding. Open access funding was provided by the Consiglio Nazionale delle Ricerche (CNR) under the CRUI-CARE Agreement.

## Author Contributions.

The main text was written by G.C. The research was designed by G.C., N.A. and N.M. On field UAV investigations were carried out by N.A., G.C., J.C., N.M., the data have been processed by D.C. and N.A., analyzed and interpreted by .C., N.A. N.M. and A.S. All authors participated in reviewing the manuscript, with N.A., N.M. and R.L. overseeing its supervision